Nano Research

Open Access

Research Article

Machine learning driven rational design of dual atom catalysts on graphene for carbon dioxide electroreduction

Dongxu Jiao[1], Xinyi Li[1], Mingzi Sun[2], Lin Liu[1], Jinchang Fan[1], Jingxiang Zhao[3], Bolong Huang[2]✉, and Xiaoqiang Cui[1]✉

[1] *State Key Laboratory of Automotive Simulation and Control, School of Materials Science and Engineering, and Key Laboratory of Automobile Materials of MOE, Jilin University, Changchun 130012, China*
[2] *Department of Applied Biology and Chemical Technology, The Hong Kong Polytechnic University, Hung Hom, Kowloon, Hong Kong, China*
[3] *College of Chemistry and Chemical Engineering, and Key Laboratory of Photonic and Electronic Bandgap Materials, Ministry of Education, Harbin Normal University, Harbin 150025, China*

Cite this article: *Nano Research*, **2025**, *18*, 94907044. https://doi.org/10.26599/NR.2025.94907044

ABSTRACT: The development of high-performance atomic catalysts for the carbon dioxide reduction reaction (CO_2RR) is a time-consuming process due to the complexity of the reaction mechanism and the uncertainty of the active site. Herein, we have proposed combining density functional theory (DFT) and machine learning (ML) to investigate the potential of topological graphene-based dual-atom catalysts (DACs) as CO_2RR electrocatalysts. By analyzing the ML results, we identify the number of d-orbital electrons in the active site as a key factor influencing the CO_2RR catalytic activity. Additionally, we propose a simple descriptor to measure the CO_2RR activity of these DACs. Our findings provide plausible explanations for the synergistic interactions between bimetallic atoms in CO_2RR and allow us to screen the homogeneous Ni-Ni pair as the most promising dual-atom catalysts. This work offers a fast ML approach based on limited DFT calculations to predict the most electroactive and stable DACs on carbon support for CO_2RR, facilitating rapid screening of high-performance dual-atom catalysts.

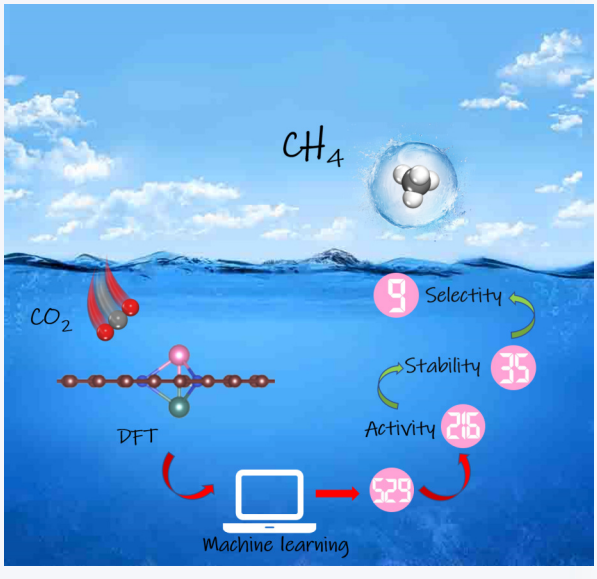

KEYWORDS: CO_2 reaction reduction, dual-atom catalysts, density functional theory, machine learning

1 Introduction

In the context of the worsening greenhouse effect, the conversion and elimination of carbon dioxide (CO_2) into valuable carbon-based chemicals is a crucial task in achieving the "dual-carbon goal" [1, 2]. To achieve the carbon neutrality goals, reducing CO_2 emissions and promoting effective conversions to high-value-added products become the research focuses of the scientific community. Among different proposed methods, electrochemical CO_2 reduction (CO_2RR) is one of the most promising approaches for achieving the carbon cycle and addressing environmental concerns, which is typically carried out at room temperature and pressure [3–6]. Despite a large body of literature on electrocatalytic CO_2RR, the development of CO_2RR electrocatalysts with high stability, activity, and selectivity remains a significant challenge due to the inert nature of CO_2 molecules and the complex CO_2RR process [7–10]. Noble metals, such as Au, Ag, Cu, Pd, and their alloys, have been considered potential electrocatalysts for CO_2RR [11–15]. However, these metal catalysts suffer from poor durabilities, low selectivities, and high overpotentials. Therefore, it is essential to develop efficient electrocatalysts for the conversion of CO_2 into diverse hydrocarbons and oxygenates.

Transition metal and nitrogen co-doped carbon-based (TM-N-C) materials have emerged as a highly promising two-dimensional (2D) nanomaterial for supporting double metal atoms, owing to

Received: August 26, 2024; **Revised:** September 18, 2024
Accepted: September 19, 2024

✉Address correspondence to Bolong Huang, bhuang@polyu.edu.hk; Xiaoqiang Cui, xqcui@jlu.edu.cn

their expansive specific surface area, excellent electrical conductivity, and remarkable stability [16, 17]. The introduction of a second metal atom in these materials enables the synergistic effects between the metal atoms, thereby effectively modulating the catalyst's electronic properties and enhancing its catalytic activity [18, 19]. As a result, dual-atom catalysts (DACs) have been extensively explored both experimentally and theoretically in various important electrocatalytic reactions [20–23]. Notably, an intriguing inverse intercalation structure has been observed in lanthanide boron clusters and has been theoretically extended to nanomaterials, leading to a novel sandwich structure [24–28]. For example, Yu et al. Li et al. showed that this type of diatomic Pt catalyst can be used as an excellent CO_2 sensor, further revealing that RhIr can be used as a CO_2RR catalyst. Wan et al. showed that Ag-Mo phthalocyanine can be used well to convert CO_2 to CO. Therefore, inspired by these works we extended this type of DAC to the TM-N-C catalysts. The metal dimer in this structure is adsorbed vertically on the substrate and protruding outwards from the substrate plane. This unique arrangement allows for efficient exposure of active sites, facilitating the activation of inert CO_2 molecules (Fig. 1(a)). Nonetheless, the selection of the most suitable dual-atom catalyst system remains challenging due to the intensive time and material costs of the experimental trial-and-error methods for the possible hundreds of dual-atom combinations.

Machine learning (ML) offers a powerful tool for large-scale materials design and screening, particularly in rapidly identifying catalysts suitable for complex reduction reactions involving multiple electrons. Traditional density functional theory (DFT) calculations also need a parallel and solid reference for benchmarking toward in-depth explorations of DACs [29–31]. By combining ML and DFT computations, it becomes possible to analyze the correlation between the intrinsic properties of catalysts and their catalytic activity using feature engineering. This approach enables comparable and referable predictions of high-performance electrocatalysts with superior electroactivity and stability, accelerating the catalyst design, and efficiently reducing computational time and costs [32, 33].

In this study, we designed a workflow that relies on three steps including (1) setting out initial data, (2) selecting machine learning models, and (3) screening suitable catalysts, which is defined as the "3S" process (corresponding to the initials of each step in the workflow). An example of N-doped topological graphene supported dual metal atoms (TMTM'@NG) for the CO_2RR is used to explore the potential of this approach combining ML and DFT. 23 transition metals were selected for combination and to evaluate the catalytic activity of these DACs through the predictions of limiting potentials for CO_2RR. Remarkably, 216 DACs exhibited superior catalytic activity compared to metal-based benchmark Cu(211) (U_L = −0.74 V) [34]. To further narrow down the selection, we conducted additional stability and selectivity investigations, ultimately identifying 9 promising CO_2RR DACs, represented by Ni-Ni pair dual metal. An intriguing finding from our study is that the activity trend of these DACs towards CO_2RR can be described by using a simple descriptor and the free energy change of OH* intermediate (ΔG_{OH^*}). This work offers important theoretical guidance for the rapid screening of CO_2RR catalysts. The combination of ML and DFT provides a powerful approach to efficiently explore the catalytic potential of dual-atom catalysts and accelerate the discovery of highly active and selective catalysts for CO_2 conversions.

2 Results and discussion

2.1 Catalytic activity of CO_2RR on 20 DACs

For CO_2RR, there are various pathways that can generate C_1 products such as CO, HCOOH, CH_3OH, and CH_4 [35, 36]. To identify the most promising DACs, the corresponding Gibbs free energy changes (ΔG) need to be obtained through the calculations of reaction trends for all possible elementary steps on the 20 selected different DACs. Based on the Gibbs free energy changes, the corresponding limiting potentials (U_L) are determined, which represents the lowest applied potential that all the reaction steps become downhill in free energy. Accordingly, the smaller absolute value of U_L directly reveals the higher catalytic activity. Although there are many possible combinations among metals, we have randomly selected 20 different combinations of DAC for the initial DFT calculations, which will act as the learning datasets for subsequent ML predictions. Our findings indicate that the most favorable reaction pathways among these 20 DACs involve

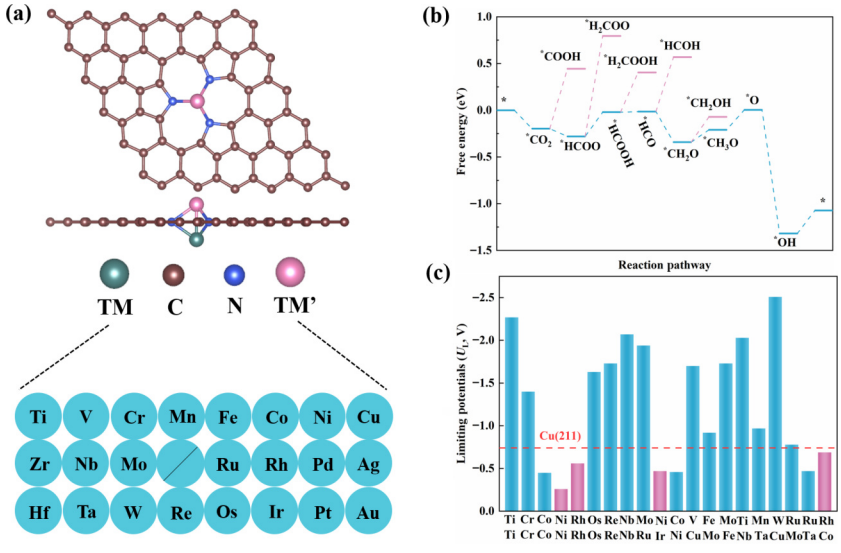

Figure 1 These two pictures are not very clear. Please provide the high-definition original figures and remove the gray box outside. This gray box has no special meaning.

converting CO_2 to CH_4 through an eight-electron reduction process (Figs. S1 and S2 in the Electronic Supplementary Material (ESM)). We take the Ni-Ni pair as an example to illustrate the corresponding CO_2RR mechanism. As depicted in Fig. 1(b), the reaction proceeds as follows: * → *CO_2 → *HCOO → *HCOOH → *CHO + H_2O → *CH_2O → *CH_3O → *O + CH_4 → *OH → H_2O (* represents the catalyst surface site). It is worth noting that the *HCOO → *HCOOH is the potential-determining step (PDS) throughout the entire CO_2RR process, as it possesses the highest ΔG value of 0.26 eV. This step also corresponds to the U_L of −0.26 V.

Additionally, in Fig. 1(c), the U_L of all 20 DAC candidates were summarized. The CO_2RR activity of these DACs was assessed by using Cu(211) as a benchmark catalyst. The results showed that the PDS for TiTi, CrCr, CoCo, OsOs, ReRe, NbNb, MoRu, CoNi, VCu, FeMo, MoFe, TiNb, MnTa, WCu, RuMo and RuTa is at *OH desorption with U_L values of −2.27, −1.40, −0.45, −1.63, −1.73, −2.07, −1.94, −0.46, −1.7, −0.92, −1.73, −2.03, −0.97, −2.51, −0.78, and −0.47 V, respectively. On the other hand, the PDS for CO_2RR on NiNi, RhRh, NiIr, and RhCo is identified as the formation of HCOOH* with U_L values of −0.26, −0.56, −0.47, and −0.69 V, respectively. Overall, the NiNi, CoCo, RhRh, NiIr, CoNi, RuTa, and RhCo catalysts exhibit high CO_2RR catalytic activity due to their lower limiting potentials compared to Cu(211).

2.2 Machine learning model training, testing, and selection

The DFT-ML process in our study can be summarized into three main steps (Fig. 2(a)). Firstly, we selected the DFT calculation results and eigenvalues as input data. Specifically, we focused on the seven intrinsic properties of metal atoms: atomic mass (M), atomic radius (R), d-orbital electrons count (θ_d), outermost electron number (N_e), atomic number (N_a), electronegativity (χ), and first ionization energy (E_i). These properties were chosen as eigenvalues for the ML model. To form the input data, we paired two metal atom eigenvalues, resulting in a total of 14 eigenvalues. Secondly, we carefully selected a ML model that effectively analyzes the input data and provides accurate predictions. Lastly, we employed ML-driven prediction methods to screen and identify the most suitable catalysts. For this purpose, we used the known limiting potential U_L as the direct descriptor for the catalytic performance of 20 DACs obtained from DFT calculations as the target values to construct the ML model. The ML model was then utilized to predict CO_2RR catalytic performance for the remaining 509 DACs.

We randomly divided the dataset into 15 training sets and 5 test sets, using a total of 20 sets of data. Five different machine learning algorithms, namely GBR, FRF, DTR, KNR, and SVR, were selected for the prediction task. Following the completion of the machine learning iterations, we determined the most appropriate R^2 and RMSE values in order to obtain accurate CO_2RR energy data output. Figure 2(b) illustrates the R^2 and RMSE values for the five different algorithms in predicting CO_2RR catalytic activity. It is evident that the GBR model outperforms the other model in terms of fitting effect. In particular, the GBR mode achieves an RMSE of 0.01 and an R^2 of 0.99 on the training set, while on the test set it achieves an RMSE of 0.11 and an R^2 of 0.97 (as shown in Fig. 2(c)). The RFR and DTR models exhibit moderate performance with respect to RMSE and R^2. The RMSE values of the training set for RFR and DTR are 0.13 and 0.01, respectively, while the RMSE values of the test set are 0.25 and 0.33. The corresponding R^2 scores for the training set are 0.97 and 0.99, and for the test set are 0.86 and 0.84. Although these results are lower than those of the GBR model, they still indicate a satisfactory level of model performance. In contrast, the SVR and KNR models demonstrate higher RMSE values and lower R^2 values, suggesting their inaccuracies. The training set RMSE values for SVR and KNR are 0.54 and 0.60, while the test set RMSE values are 0.84 and 0.78. The corresponding R^2 values for the training set are 0.32 and 0.10, and for the test set, they are 0.05 and 0.08. In conclusion, the prediction

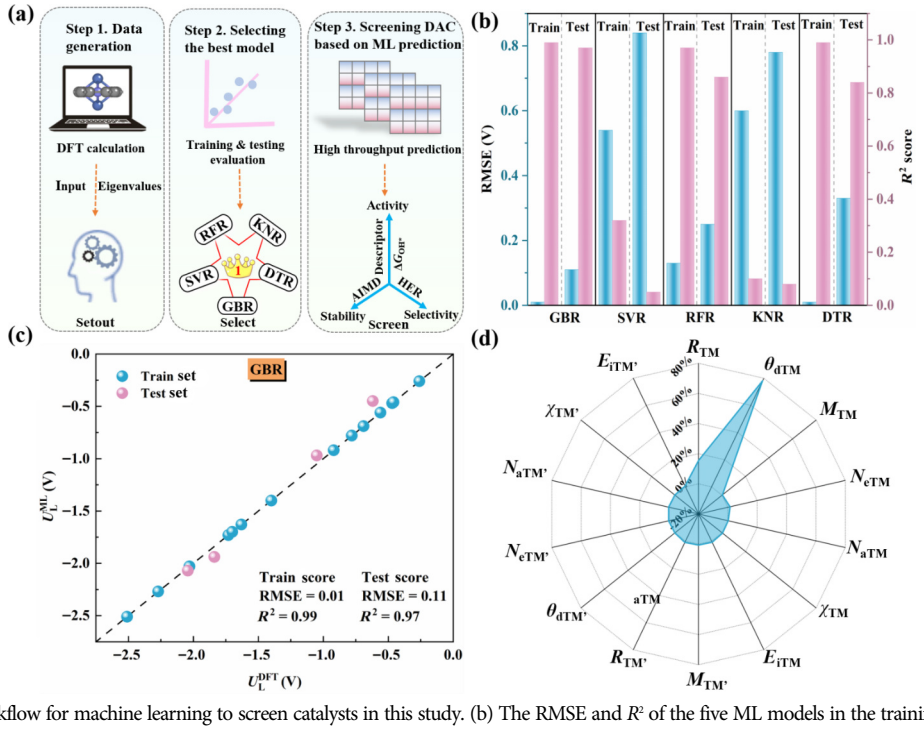

Figure 2 (a) Overall workflow for machine learning to screen catalysts in this study. (b) The RMSE and R^2 of the five ML models in the training and test sets, (c) the U_L of the GBR model predicted and DFT calculation is compared, and (d) the feature importance predicted by the GBR model.

of CO_2RR activity using the trained GBR model is considered reliable. Therefore, we select the GBR model to further predict the catalytic performance of other DACs.

The feature importance in GBR models for predicting CO_2RR is depicted in Fig. 2(d). Among these features, θ_{dTM} (78.04%) stands out as the most important one, as it relates to the metal sites' capability to accept lone pair electrons from free molecules. Additionally, R_{TM} is also an important feature of the prediction, which shows a correlation of 15.47% with the predicted outcomes of the limiting potential. Together, these two eigenvalues hold a total weight of 93.51% and serve as the most important two features for ML to achieve accurate predictions of limiting potentials for CO_2RR performances. Conversely, the other eigenvalues have minimal impact on the prediction results. Consequently, the ML training is performed with DFT calculations to effectively guide the rational design of efficient electrocatalysts, prioritizing the prediction of the catalysts' catalytic performance.

2.3 Machine learning prediction and DFT verification

Learning Prediction and DFT Verification. Based on the obtained GBR model, the CO_2RR catalytic performance of the remaining 509 DACs was predicted. The predicted U_L values of CO_2RR for these DACs are visualized as a heat map in Fig. 3(a). The color gradient represents the U_L values, with dark red indicating lower U_L and dark blue indicating higher U_L. The results indicate that out of the 529 DACs, 216 DACs exhibited U_L values below −0.74 V, 53 DACs had U_L values below −0.5 V, and 18 DACs had U_L values below −0.4 V. Specifically, Ni- and Co-based DACs demonstrated less negative U_L values ranging from −0.26 to −0.47 V (Ni-based) and −0.36 to −0.58 V (Co-based). Notably, the DACs with the Ni-Ni combination exhibited the least negative U_L of −0.26 V.

To validate the accuracy of the ML prediction results, 10 DACs were selected and their CO_2RR performance was verified using the DFT calculations. As depicted in Fig. 3(b), the ML predictions align well with the DFT calculations, with an average error of only 0.03 V. The DFT results identify NiTi as the best CO_2RR catalyst among the 10 selected DACs (U_L = −0.37 V), which closely matches the ML prediction of −0.36 V. Similarly, the other 9 DACs (such as NiMn, RhZr, and CuFe) also exhibit excellent agreement between the DFT and ML predictions. Overall, we have successfully predicted 216 high-performance CO_2RR catalysts out of 529 DACs with an extremely low average error of 0.03 V by combining DFT and ML methods. Compared to the pure DFT calculations, this DFT-ML combined strategy offers significantly faster computational speed, higher prediction accuracy, and reduced computational costs, enabling rapid and rational catalyst development. Based on the feature engineering and activity prediction in ML, a descriptor (φ) can be determined using the equation: $\varphi = (\theta_{dTM} \times N_{eTM})^2/(R_{TM} + R_{TM'})$. The U_L values of these candidates show a strong correlation with φ, with an R^2 value of 0.89 (Fig. 3(c)). Thus, by leveraging feature engineering and ML-based descriptor determination, we are able to realize the efficient screening of TM-TM'@NG catalysts for CO_2RR, without relying on complex DFT calculations.

2.4 Stability of 216 DACs

The stability of 216 DACs was evaluated using formation energy (E_{form}) and dissolution potential (U_{diss}) as shown in Fig. 4(a) [37, 38]. Notably, the stability of these candidates was evaluated by considering both U_{diss} and E_{form} criteria. To determine the stability of these materials in a more detailed and precise manner, therefore, only DFT was used for the evaluation of stability while no data of machine learning was used. Positive E_{form} values indicated lower thermodynamic stability, while negative U_{diss} values indicated instability in an electrochemical environment. Based on these criteria, 35 DACs with high thermodynamic and electrochemical stabilities were identified. To further confirm the thermodynamic stability of these 35 DACs, AIMD simulations were performed (Figs. 4(b) and 4(c), and Figs. S3 and S4 in the ESM). The results showed that 9 DACs maintained their complete structures during the simulations at 300 K for 5 ps, indicating good thermodynamic stability. However, the remaining 26 DACs exhibited significant deformation in their configurations, suggesting lower thermodynamic stability (Figs. S3 and S4 in the ESM).

2.5 Competition HER and the effect of solvation on 9 DACs

In general, the competing reaction for CO_2RR is the hydrogen

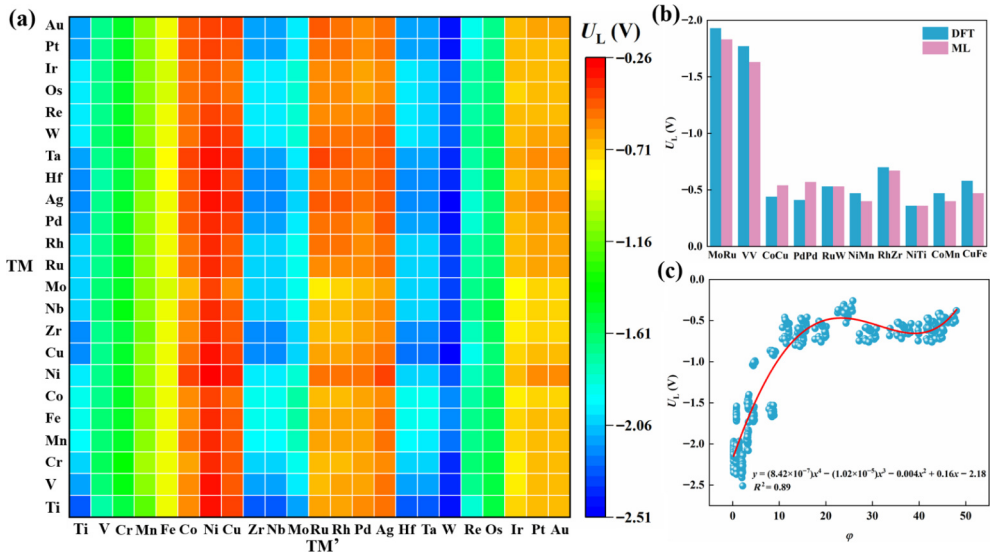

Figure 3 (a) ML predicted the U_L of 529 DACs. (b) DFT calculations validated 10 DACs with lower U_L predicted by ML. (c) The relationship between the descriptor and the limiting potential.

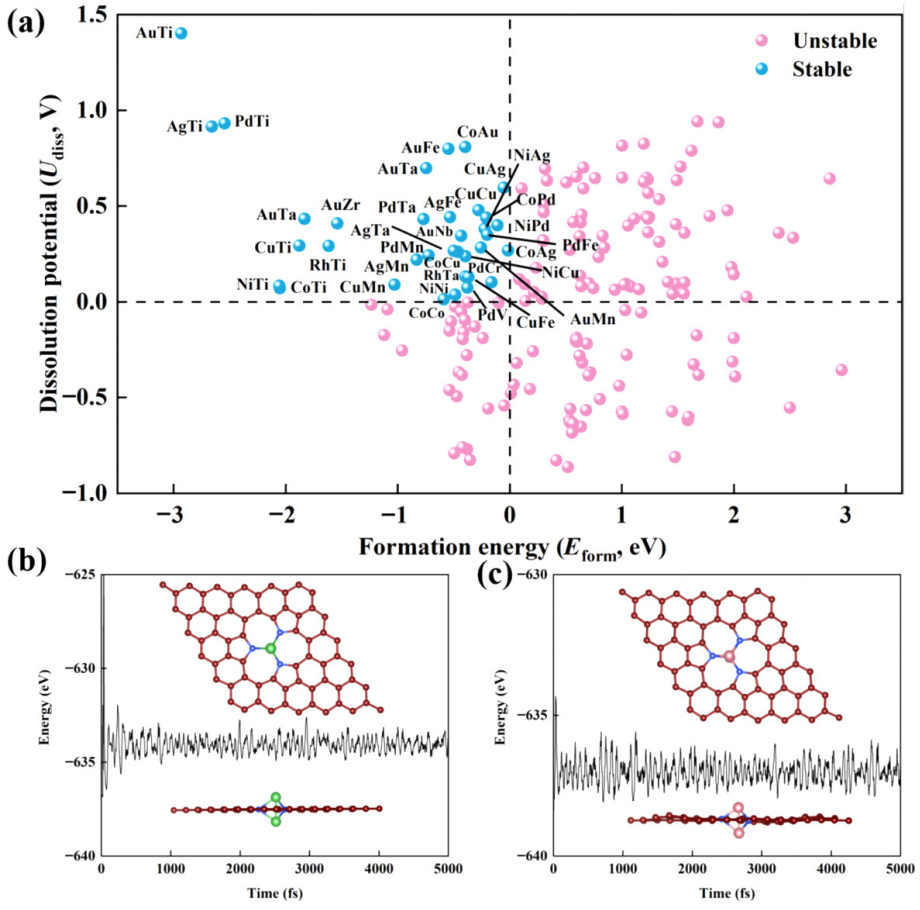

Figure 4 (a) Computed formation energy and dissolution potential of 216 DACs. (b) and (c) AIMD energy distributions of NiNi and CoCo at 300 K, respectively (optimized final structure (FS) as the insert).

evolution reaction (HER) [39]. To assess the selectivity of CO_2RR, we compared the adsorption energies of H* and CO_2* on the screened 9 different DACs with high stability after MD simulations. The results, shown in Fig. 5(a), indicate that the adsorption energy of CO_2* ($E_{ads}(CO_2*)$) is much more negative than that of H* ($E_{ads}(H*)$) on these 9 DACs. This suggests that the H* adsorption is greatly suppressed, leading to a suppression of HER and indicating a high selectivity for CO_2RR. Since the electrochemical CO_2RR is in an aqueous solution, we used the VASPsol implicit solvation model to default include the effects of solvation on catalytic activity [40]. As depicted in Fig. 5(b), the final products of these catalysts were all CH_4, with respective overpotentials (U_L) of −0.29, −0.28, −0.38, −0.63, −0.66, −0.73, −0.31, −0.98 and −0.48 V. These values are nearly consistent with those obtained without taking account of solvation effects.

2.6 CO_2RR activity origin

The initial investigation focused on the adsorption and activation of CO_2 molecules on a specific DAC, which is essential for CO_2RR [41]. The analysis of charge density difference and Bader charge revealed a substantial transfer of charge to the adsorbed CO_2 through the TM–C and TM–O bonds. This resulted in a bending of the CO_2 molecule from 180° to an angle range of 144.1° to 157.3°, along with elongation of the C–O bond length from 1.18 Å (gas phase) to 1.21–1.27 Å (Fig. 6(a) and Fig. S5 in the ESM). This supports the successful activation of inert CO_2, which is polarized to promote chemisorption and further transformation to other intermediates. To gain further insights into the CO_2 activation mechanism on these DACs, we calculated the partial densities of states (PDOSs) and crystal orbital Hamilton populations (COHP). The results indicated a clear hybridization between the d-orbital of the metal atoms and CO_2 molecular orbitals, highlighting a strong interaction between them (Fig. 6(b) and Fig. S6 in the ESM). Additionally, the COHP analysis demonstrated that the interaction between the metal d-orbitals and the CO_2 molecular orbitals led to the formation of partially occupied states. The integrated crystal orbital Hamilton populations (ICOHP) ranged from −0.65 to −1.31, confirming the significant interactions between CO_2 and the DACs and suggesting the ability of these DACs to activate CO_2 [42].

Interestingly, a subtle correlation between the adsorption free energy of OH* (ΔG_{OH*}) and the CO_2RR activity trend of the different DACs can be observed. This relationship is depicted in Fig. 6(c), where a volcano plot of the limiting potential on these DACs is presented. Notably, CuMn, CuFe, and CuCu were not considered due to their poor correlation with ΔG_{OH*}, however, this has little or no effect on the conclusions. As expected, NiNi falls near the peak of the volcano, indicating its high activity attributed to its optimal adsorption strength with OH* species. In contrast, when ΔG_{OH*} is high with a weak adsorption trend of *OH, the hydrogenation step of HCOO* becomes the PDS. Conversely, if the adsorption is too strong, the higher free energy barrier for OH* desorption also leads to a decrease in catalytic activity. Based on the above results, contour plots of the limiting potential as a function of

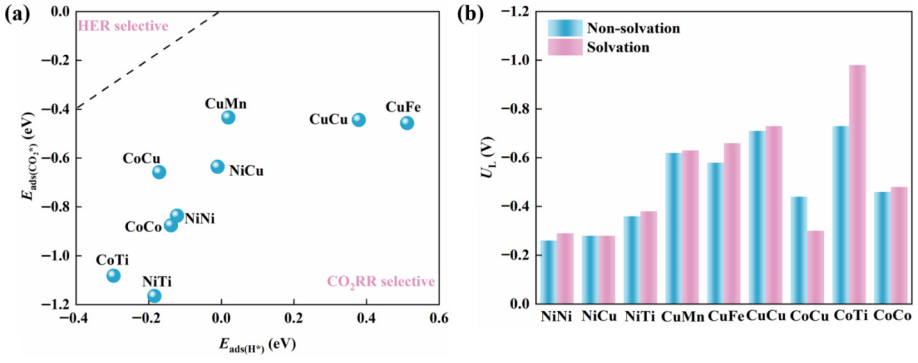

Figure 5 (a) Comparison of adsorption energy of CO_2 and H*. (b) U_L comparison of 9 DACs under solvation conditions was considered.

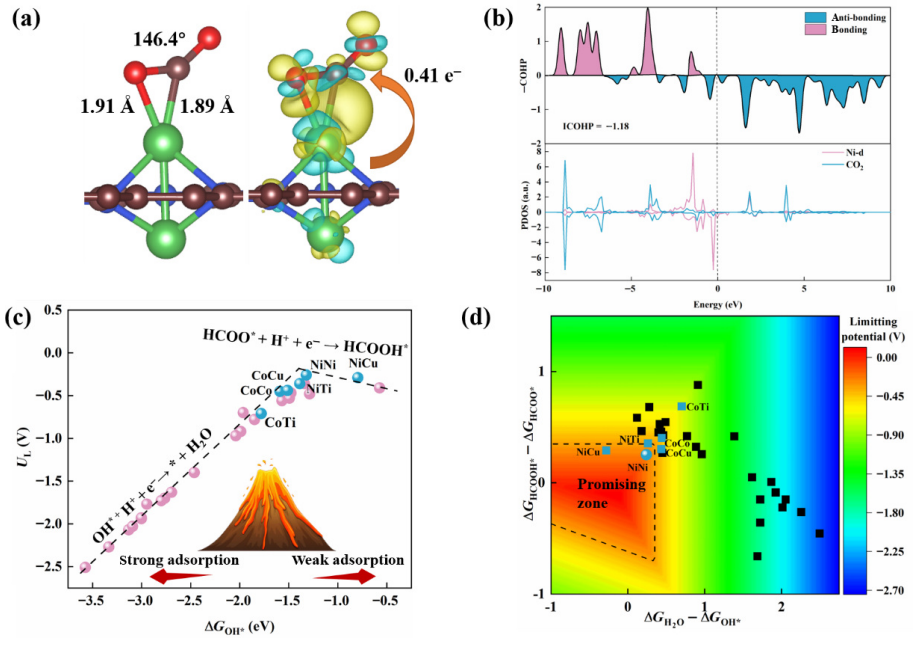

Figure 6 (a) The most stable CO_2 adsorption structure and charge density difference, (b) PDOS and COHP for CO_2 adsorbed on NiNi, (c) a volcano plot of DACs between the ΔG_{OH^*} and limiting potentials, and (d) a contour plot of U_L as a function of two potential-determining steps ($OH^* + H^+ + e^- \rightarrow H_2O + *$ and $HCOO^* + H^+ + e^- \rightarrow HCOOH^*$).

the two PDSs ($OH^* + H^+ + e^- \rightarrow H_2O + *$ and $HCOO^* + H^+ + e^- \rightarrow HCOOH^*$) are plotted in Fig. 6(d). Notably, the Ni-Ni DACs still fall within the promising region of low U_L ($-0.35 < U_L < 0$ V), further emphasizing its potential as a catalyst for CO_2RR.

3 Conclusion

In summary, we have successfully employed a hybrid DFT-ML computational approach to efficiently screen and identify possible dual metal combinations for DACs that potentially have high catalytic activity for CH_4 formation by CO_2RR. Out of the initial pool of 529 DAC candidates, 20 structures were selected as input data for ML, and the catalytic performance of the remaining 509 structures was accurately predicted using the GBR algorithm. By considering factors such as activity, stability, and selectivity, we were able to identify 9 DACs as highly efficient catalysts for CO_2RR. Additionally, the ML results also reveal that the TM d-orbital electron is one of the most dominant features in realizing the accurate predictions of limiting potentials for CO_2RR. It is worth noting that two key factors, namely a newly proposed descriptor based on the intrinsic properties of metal atoms and the adsorption free energy of the key intermediate ΔG_{OH^*}, could effectively describe the catalytic activity of CO_2RR on these DACs. Overall, this work not only enhances our understanding of the CO_2RR mechanism but also offers new strategies for the rapid identification of high-performance catalysts for CO_2RR.

4 Methods

4.1 DFT calculations

All DFT calculations were performed using the Vienna *ab initio* simulation package (VASP), employing a plane-wave basis set [43]. The projector augmented wave (PAW) method was utilized to describe electrons and ions interactions [44, 45]. The exchange-correlation interactions were determined by the Perdew–Burke–Ernzerhof (PBE) functional and generalized gradient approximation (GGA) [46]. Grimme's scheme (DFT+D3) method was applied to incorporate an empirical correction for van der Waals (vdW) interaction [47]. A cutoff energy of 500 eV was employed, and the convergence criterion for the residual force and energy was set to 0.02 eV·Å^{-1} and 10^{-5} eV, respectively. A vacuum

space of 15 Å in the *z*-direction was used to prevent interactions between periodic images. The Brillouin zone was sampled using a Monkhorst-Pack mesh with 3 × 3 × 1 k-points throughout the calculations.

Additionally, *ab initio* molecular dynamics (AIMD) simulations were conducted in the canonical ensemble (NVT) with Nose–Hoover thermostat at 300 K since we expect the lattice size of the DAC to remain unchanged in the AIMD simulations. Before the AIMD simulations, the structures of all the DACs have been fully optimized. The simulations were carried out for 5 ps to evaluate the thermodynamic stability of DACs [48, 49].

The binding energy of TM and TM' atoms on the pyrrolic N-doped defective graphene are defined as follows

$$E_{b\text{-}TM} = E_{TM@NG} - E_{NG} - E_{TM} \quad (1)$$

$$E_{b\text{-}TM'} = E_{TMTM'@NG} - E_{TM@NG} - E_{TM'} \quad (2)$$

where $E_{TMTM'@NG}$, $E_{TM@NG}$ and E_{NG} represents the total energy of the TMTM'@NG, TM@NG and NG, respectively. E_{TM} and $E_{TM'}$ refer to free TM and TM' atom energy. The cohesive energy in the metalloid phase of metal (E_{coh}) is defined as follows

$$E_{coh\text{-}TM/TM'} = E_{TM/TM'(bulk)} - E_{TM/TM'(free)} \quad (3)$$

where $E_{TM/TM'(bulk)}$ and $E_{TM/TM'(free)}$ are the energy of TM/TM' in its bulk and free state.

The formation energy (E_{form}) of TMTM'@NG was defined as follows

$$E_{form} = (E_{TMTM'@NG} - E_{NG} - E_{TM'(bulk)} - E_{TM(bulk)})/2 \quad (4)$$

According to Eqs. (1) to (4), E_{form} can be obtained from the following formula: $E_{form} = \overline{E_b} - \overline{E_{coh}}$, in which the bars denote average energies for TM and TM'. The dissolution potential (U_{diss}) was calculated as follows: $U_{diss} = (U^o_{diss(TM)} + U^o_{diss(TM')})/2 - E_{form}/ne$, where $U^o_{diss(TM)}/U^o_{diss(TM')}$, E_{from} and n are the standard dissolution potential of bulk TM/TM', the formation energy of the catalyst, and the number of electrons involved in the dissolution.

The adsorption energy (E_{ads}) of various intermediates during the CO_2RR on these DACs can be obtained as the following equation: $E_{ads} = E_{total} - E_{adsorbate} - E_{DACs}$, in which the E_{total}, $E_{adsorbate}$, and E_{DACs} represent the total energy of the adsorbed species on DACs, the isolated CO_2RR intermediate, and the DACs, respectively. According to this definition, a more negative E_{ads} represents a stronger adsorption. The change in the Gibbs free energy (ΔG) of each elementary step was computed by the computational hydrogen electrode (CHE) model [34, 50]. Based on this model, the ΔG value can be computed by: $\Delta G = \Delta E + \Delta E_{ZPE} - T\Delta S$ where ΔE is the reaction energy difference, which can be directly obtained by analyzing the DFT total energies. The zero-point energy difference (ΔE_{ZPE}) between the product and the reactant can be derived by computing the corresponding vibrational frequencies. ΔS is the change in entropy between the product and the reactant at room temperature (T = 298.15 K). Based on the obtained free energy changes of each elementary step, the limiting potential (U_L) was further computed as follows: $U_L = -\max(\Delta G_1, \Delta G_2, \Delta G_3, \Delta G_4, ..., \Delta G_i)/e$, and a lower U_L suggests a higher CO_2RR activity.

4.2 ML method

All the ML algorithms were employed to predict the U_L of CO_2RR in Python3 environment by using Scikit-learn package [51], including *k*-Neighbor Regression (KNR), Support Vector Regression (SVR), Decision Tree Regression (DTR), Gradient Boosted Regression (GBR) and Random Forest Regression (RFR) [52–56]. The input data used for DFT was randomly divided into training and test sets in 4:1. The coefficient of determination (R^2) and root-mean-square error (RMSE) to evaluate the model accuracy. R^2 and RMSE are expected to be close to 1 and as small as possible for the ideal model, respectively.

Electronic Supplementary Material: Supplementary material (further details of the theoretical calculation models, CO_2 adsorption geometries and corresponding charge density differences) is available in the online version of this article at https://doi.org/10.26599/NR.2025.94907044.

Data availability

All data needed to support the conclusions in the paper are presented in the manuscript and the Electronic Supplementary Material. Additional data related to this paper may be requested from the corresponding author upon request.

Acknowledgements

This work was financially supported by the National Natural Science Foundation of China (Nos. 12034002, 22279044, and 22202080), the Jilin Province Science and Technology Development Program (No. 20210301009GX), Research Grant Council of Hong Kong (No. 15304023), National Natural Science Foundation of China/Research Grant Council of Hong Kong Joint Research Scheme (No. N_PolyU502/21), National Natural Science Foundation of China/Research Grants Council of Hong Kong Collaborative Research Scheme (No. CRS_PolyU504/22), the funding for Projects of Strategic Importance of The Hong Kong Polytechnic University (Project Code: 1-ZE2V), Shenzhen Fundamental Research Scheme-General Program (No. JCYJ20220531090807017), and Natural Science Foundation of Guangdong Province (No. 2023A1515012219).

Declaration of competing interest

All the contributing authors report no conflict of interests in this work.

Author contributions

D. X. J.: Data curation, writing manuscript, experimental design. X. Y. L.: Data curation. M. Z. S.: Writing manuscript. L. L.: Data curation. J. C. F.: Writing manuscript. J. X. Z.: Writing manuscript. B. L. H.: Project administration, funding acquisition, writing manuscript. X. Q. C.: Project administration, funding acquisition, writing manuscript. All the authors have approved the final manuscript.

Use of AI statement

None.

References

[1] Zhou, K. B.; Wang, X.; Sun, X. M.; Peng, Q.; Li, Y. D. Enhanced catalytic activity of ceria nanorods from well-defined reactive crystal planes. *J. Catal.* **2005**, *229*, 206–212.

[2] Sun, M. Z.; Wong, H. H.; Wu, T.; Lu, Q. Y.; Lu, L.; Chan, C. H.; Chen, B. A.; Dougherty, A. W.; Huang, B. L. Double-dependence correlations in graphdiyne-supported atomic catalysts to promote CO_2RR toward the generation of C2 products. *Adv. Energy Mater.* **2023**, *13*, 2203858.

[3] Chen, Z. W.; Gariepy, Z.; Chen, L. X.; Yao, X.; Anand, A.; Liu, S. J.; Tetsassi Feugmo, C. G.; Tamblyn, I.; Singh, C. V. Machine-learning-driven high-entropy alloy catalyst discovery to circumvent the scaling relation for CO_2 reduction reaction. *ACS Catal.* **2022**, *12*, 14864–14871.

[4] Zhu, Q.; Gu, Y. M.; Liang, X. Y.; Wang, X. Z.; Ma, J. A machine learning model to predict CO_2 reduction reactivity and products transferred from metal-zeolites. *ACS Catal.* **2022**, *12*, 12336–12348.

[5] Ding, H.; Shi, Y. W.; Li, Z. Y.; Wang, S.; Liang, Y. J.; Feng, H. S.; Deng, Y.; Song, X.; Pu, P. X.; Zhang, X. Active learning accelerating to screen dual-metal-site catalysts for electrochemical carbon dioxide reduction reaction. *ACS Appl. Mater. Inter.* **2023**, *15*, 12986–12997.

[6] Ding, C.; Lu, X. X.; Tao, B.; Yang, L. Q.; Xu, X. Y.; Tang, L. Q.; Chi, H. Q.; Yang, Y.; Meira, D. M.; Wang, L. et al. Interlayer spacing regulation by single-atom indium$^{\delta+}$-N_4 on carbon nitride for boosting CO_2/CO photo-conversion. *Adv. Funct. Mater.* **2023**, *33*, 2302824.

[7] Hu, S.; Qiao, P. Z.; Yi, X. L.; Lei, Y. M.; Hu, H. L.; Ye, J. H.; Wang, D. F. Selective photocatalytic reduction of CO_2 to CO mediated by silver single atoms anchored on tubular carbon nitride. *Angew. Chem., Int. Ed.* **2023**, *62*, e202304585.

[8] Jiang, J. W.; Wang, X. F.; Guo, H. Enhanced interfacial charge transfer/separation by lspr-induced defective semiconductor toward high CO_2RR performance. *Small* **2023**, *19*, 2301280.

[9] Miao, Q. Y.; Lu, C. B.; Xu, Q.; Yang, S.; Liu, M. H.; Liu, S. J.; Yu, C. B.; Zhuang, X. D.; Jiang, Z.; Zeng, G. F. CoN_2O_2 sites in carbon nanosheets by template-pyrolysis of COFs for CO_2RR. *Chem. Eng. J.* **2022**, *450*, 138427.

[10] Sun, M. Z.; Wong, H. H.; Wu, T.; Dougherty, A. W.; Huang, B. L. Stepping out of transition metals: Activating the dual atomic catalyst through main group elements. *Adv. Energy Mater.* **2021**, *11*, 2101404.

[11] Mu, S. J.; Lu, H. L.; Wu, Q. B.; Li, L.; Zhao, R. J.; Long, C.; Cui, C. H. Hydroxyl radicals dominate reoxidation of oxide-derived cu in electrochemical CO_2 reduction. *Nat. Commun.* **2022**, *13*, 3694.

[12] Hai, G. T.; Xue, X. D.; Feng, S. H.; Ma, Y. W.; Huang, X. B. High-throughput computational screening of metal-organic frameworks as high-performance electrocatalysts for CO_2RR. *ACS Catal.* **2022**, *12*, 15271–15281.

[13] Lei, Q.; Huang, L.; Yin, J.; Davaasuren, B.; Yuan, Y. Y.; Dong, X. L.; Wu, Z. P.; Wang, X. Q.; Yao, K. X.; Lu, X. et al. Structural evolution and strain generation of derived-Cu catalysts during CO_2 electroreduction. *Nat. Commun.* **2022**, *13*, 4857.

[14] Xie, W. B.; Xu, J. S.; Md Idros, U.; Katsuhira, J.; Fuki, M.; Hayashi, M.; Yamanaka, M.; Kobori, Y.; Matsubara, R. Metal-free reduction of CO_2 to formate using a photochemical organohydride-catalyst recycling strategy. *Nat. Chem.* **2023**, *15*, 794–802.

[15] Timoshenko, J.; Bergmann, A.; Rettenmaier, C.; Herzog, A.; Arán-Ais, R. M.; Jeon, H. S.; Haase, F. T.; Hejral, U.; Grosse, P.; Kühl, S. et al. Steering the structure and selectivity of CO_2 electroreduction catalysts by potential pulses. *Nat. Catal.* **2022**, *5*, 259–267.

[16] Shi, R.; Guo, J. H.; Zhang, X. R.; Waterhouse, G. I. N.; Han, Z. J.; Zhao, Y. X.; Shang, L.; Zhou, C.; Jiang, L.; Zhang, T. R. Efficient wettability-controlled electroreduction of CO_2 to CO at Au/C interfaces. *Nat. Commun.* **2020**, *11*, 3028.

[17] Xie, H.; Wang, T. Y.; Liang, J. S.; Li, Q.; Sun, S. H. Cu-based nanocatalysts for electrochemical reduction of CO_2. *Nano Today* **2018**, *21*, 41–54.

[18] Xiong, L. K.; Zhang, X.; Chen, L.; Deng, Z.; Han, S.; Chen, Y. F.; Zhong, J.; Sun, H.; Lian, Y. B.; Yang, B. Y. et al. Geometric modulation of local CO flux in Ag@Cu_2O nanoreactors for steering the CO_2RR pathway toward high-efficacy methane production. *Adv. Mater.* **2021**, *33*, 2101741.

[19] Zeng, J. C.; Zhang, W. B.; Yang, Y.; Li, D.; Yu, X.; Gao, Q. S. Pd–Ag alloy electrocatalysts for CO_2 reduction: Composition tuning to break the scaling relationship. *ACS Appl. Mater. Inter.* **2019**, *11*, 33074–33081.

[20] Su, X. S.; Sun, Y. M.; Jin, L.; Zhang, L.; Yang, Y.; Kerns, P.; Liu, B.; Li, S. Z.; He, J. Hierarchically porous Cu/Zn bimetallic catalysts for highly selective CO_2 electroreduction to liquid C_2 products. *Appl. Catal. B: Environ.* **2020**, *269*, 118800.

[21] Jiang, Y. Q.; Sung, Y.; Choi, C.; Joo Bang, G.; Hong, S.; Tan, X. Y.; Wu, T. S.; Soo, Y. L., Xiong, P.; Li, M. M. J. et al. Single-atom molybdenum-N_3 sites for selective hydrogenation of CO_2 to CO. *Angew. Chem., Int. Ed.* **2022**, *61*, e202203836.

[22] Tang, Y. N.; Zhang, H. Q.; Chen, W. G.; Li, Z. H.; Liu, Z. Y.; Teng, D.; Dai, X. Q. Modulating geometric, electronic, gas sensing and catalytic properties of single-atom pd supported on divacancy and n-doped graphene sheets. *Appl. Surf. Sci.* **2020**, *508*, 145245.

[23] Cheng, D. F.; Zhao, Z. J.; Zhang, G.; Yang, P. P.; Li, L. L.; Gao, H.; Liu, S. H.; Chang, X.; Chen, S.; Wang, T. et al. The nature of active sites for carbon dioxide electroreduction over oxide-derived copper catalysts. *Nat. Commun.* **2021**, *12*, 395.

[24] Zhang, W. Y.; Chao, Y. G.; Zhang, W. S.; Zhou, J. H.; Lv, F.; Wang, K.; Lin, F. X.; Luo, H.; Li, J.; Tong, M. P. et al. Emerging dual-atomic-site catalysts for efficient energy catalysis. *Adv. Mater.* **2021**, *33*, 2102576.

[25] Ying, Y. R.; Luo, X.; Qiao, J. L.; Huang, H. T. "More is different:" synergistic effect and structural engineering in double-atom catalysts. *Adv. Funct. Mater.* **2021**, *31*, 2007423.

[26] He, T. W.; Santiago, A. R. P.; Kong, Y. C.; Ahsan, M. A.; Luque, R.; Du, A. J.; Pan, H. Atomically dispersed heteronuclear dual-atom catalysts: A new rising star in atomic catalysis. *Small* **2022**, *18*, 2106091.

[27] Wang, J.; Zhao, C. X.; Liu, J. N.; Song, Y. W.; Huang, J. Q.; Li, B. Q. Dual-atom catalysts for oxygen electrocatalysis. *Nano Energy* **2022**, *104*, 107927.

[28] Rehman, F.; Kwon, S.; Musgrave, C. B.; Tamtaji, M.; Goddard, W. A.; Luo, Z. T. High-throughput screening to predict highly active dual-atom catalysts for electrocatalytic reduction of nitrate to ammonia. *Nano Energy* **2022**, *103*, 107866.

[29] Chen, T. T.; Li, W. L.; Li, J.; Wang, L. S. $[La(\eta^x\text{-}B_x)La]^-$ (x = 7–9): A new class of inverse sandwich complexes. *Chem. Sci.* **2019**, *10*, 2534–2542.

[30] Li, W. L.; Chen, T. T.; Xing, D. H.; Chen, X.; Li, J.; Wang, L. S. Observation of highly stable and symmetric lanthanide octa-boron inverse sandwich complexes. *Proc. Natl. Acad. Sci. USA* **2018**, *115*, E6972–E6977.

[31] Lu, X. Q.; Zhao, X. N.; Mu, Y. W.; Li, S. D. Lanthanide/actinide boride nanoclusters and nanomaterials based on boron frameworks consisting of conjoined B_n rings (n = 7–9). *Phys. Chem. Chem. Phys.* **2022**, *24*, 21078–21084.

[32] Yu, L. K.; Li, F. Y.; Huang, J. S.; Sumpter, B. G.; Mustain, W. E.; Chen, Z. F. Double-atom catalysts featuring inverse sandwich structure for CO_2 reduction reaction: A synergetic first-principles and machine learning investigation. *ACS Catal.* **2023**, *13*, 9616–9628.

[33] Wan, X. H.; Zhang, Z. F.; Niu, H.; Yin, Y. H.; Kuai, C. G.; Wang, J.; Shao, C.; Guo, Y. Z. Machine-learning-accelerated catalytic activity predictions of transition metal phthalocyanine dual-metal-site catalysts for CO_2 reduction. *J. Phys. Chem. Lett.* **2021**, *12*, 6111–6118.

[34] Peterson, A. A.; Abild-Pedersen, F.; Studt, F.; Rossmeisl, J.; Nørskov, J. K. How copper catalyzes the electroreduction of carbon dioxide into hydrocarbon fuels. *Energy Environ. Sci.* **2010**, *3*, 1311–1315.

[35] Tang, T. M.; Wang, Z. L.; Guan, J. Q. Optimizing the electrocatalytic selectivity of carbon dioxide reduction reaction by regulating the electronic structure of single-atom M–N–C materials. *Adv. Funct. Mater.* **2022**, *32*, 2111504.

[36] Lai, W. C.; Qiao, Y.; Zhang, J. W.; Lin, Z. Q.; Huang, H. W. Design strategies for markedly enhancing energy efficiency in the

electrocatalytic CO_2 reduction reaction. *Energy Environ. Sci.* **2022**, *15*, 3603–3629.

[37] Guo, X. Y.; Gu, J. X.; Lin, S. R.; Zhang, S. L.; Chen, Z. F.; Huang, S. P. Tackling the activity and selectivity challenges of electrocatalysts toward the nitrogen reduction reaction via atomically dispersed biatom catalysts. *J. Am. Chem. Soc.* **2020**, *142*, 5709–5721.

[38] Song, X.; Li, Z. H.; Sheng, L.; Xiao, N. Asymmetrical radial strain energy strategy of M–N–SWCNT single atom catalysts for highly efficient hydrogen evolution: A high-throughput DFT study. *Appl. Surf. Sci.* **2023**, *639*, 158225.

[39] Saha, P.; Amanullah, S.; Dey, A. Selectivity in electrochemical CO_2 reduction. *Acc. Chem. Res.* **2022**, *55*, 134–144.

[40] Mathew, K.; Sundararaman, R.; Letchworth-Weaver, K.; Arias, T. A.; Hennig, R. G. Implicit solvation model for density-functional study of nanocrystal surfaces and reaction pathways. *J. Chem. Phys.* **2014**, *140*, 084106.

[41] Hassan, A.; Anis, I.; Shafi, S.; Assad, A.; Rasool, A.; Khanam, R.; Bhat, G. A.; Krishnamurty, S.; Dar, M. A. First-principles investigation of the electrocatalytic reduction of CO_2 on zirconium-based single-, double-, and triple-atom catalysts anchored on a graphitic carbon nitride monolayer. *ACS Appl. Nano Mater.* **2022**, *5*, 15409–15417.

[42] Ren, M. M.; Guo, X. Y.; Zhang, S. L.; Huang, S. P. Design of graphdiyne and holey graphyne-based single atom catalysts for CO_2 reduction with interpretable machine learning. *Adv. Funct. Mater.* **2023**, *33*, 2213543.

[43] Kresse, G.; Furthmüller, J. Efficient iterative schemes for *ab initio* total-energy calculations using a plane-wave basis set. *Phys. Rev. B* **1996**, *54*, 11169–11186.

[44] Blöchl, P. E. Projector augmented-wave method. *Phys. Rev. B* **1994**, *50*, 17953–17979.

[45] Kresse, G.; Joubert, D. From ultrasoft pseudopotentials to the projector augmented-wave method. *Phys. Rev. B* **1999**, *59*, 1758–1775.

[46] Perdew, J. P.; Burke, K.; Ernzerhof, M. Generalized gradient approximation made simple. *Phys. Rev. Lett.* **1996**, *77*, 3865–3868.

[47] Grimme, S. Semiempirical GGA-type density functional constructed with a long-range dispersion correction. *J. Comput. Chem.* **2006**, *27*, 1787–1799.

[48] Kresse, G.; Hafner, J. *Ab initio* molecular dynamics for liquid metals. *Phys. Rev. B* **1993**, *47*, 558–561.

[49] Nosé, S. A unified formulation of the constant temperature molecular dynamics methods. *J. Chem. Phys.* **1984**, *81*, 511–519.

[50] Nørskov, J. K.; Rossmeisl, J.; Logadottir, A.; Lindqvist, L.; Kitchin, J. R.; Bligaard, T.; Jónsson, H. Origin of the overpotential for oxygen reduction at a fuel-cell cathode. *J. Phys. Chem. B* **2004**, *108*, 17886–17892.

[51] Pedregosa, F.; Varoquaux, G.; Gramfort, A.; Michel, V.; Thirion, B.; Grisel, O.; Blondel, M.; Prettenhofer, P.; Weiss, R.; Dubourg, V. et al. Scikit-learn: Machine learning in python. *J. Mach. Learn. Res.* **2011**, *12*, 2825–2830.

[52] Chen, A.; Zhang, X.; Chen, L. T.; Yao, S.; Zhou, Z. A machine learning model on simple features for CO_2 reduction electrocatalysts. *J. Phys. Chem. C* **2020**, *124*, 22471–22478.

[53] Seko, A.; Maekawa, T.; Tsuda, K.; Tanaka, I. Machine learning with systematic density-functional theory calculations: Application to melting temperatures of single- and binary-component solids. *Phys. Rev. B* **2014**, *89*, 054303.

[54] Jiao, D. X.; Zhang, D. T.; Wang, D. W.; Fan, J. C.; Ma, X. C.; Zhao, J. X.; Zheng, W. T.; Cui, X. Q. Applying machine-learning screening of single transition metal atoms anchored on N-doped γ-graphyne for carbon monoxide electroreduction toward C_1 products. *Nano Res.* **2023**, *16*, 11511–11520.

[55] Yang, L.; Fan, J. K.; Xiao, B. B.; Zhu, W. H. Unveiling "sabatier principle" for electrocatalytic nitric oxide reduction on single cluster catalysts: A DFT and machine learning guideline. *Chem. Eng. J.* **2023**, *468*, 143823.

[56] Abraham, B. M.; Sinha, P.; Halder, P.; Singh, J. K. Fusing a machine learning strategy with density functional theory to hasten the discovery of 2D mxene-based catalysts for hydrogen generation. *J. Mater. Chem. A* **2023**, *11*, 8091–8100.